Covalent Organic Frameworks Hot Paper

How to cite:
International Edition: doi.org/10.1002/anie.202213106
German Edition: doi.org/10.1002/ange.202213106

Electrochemical Double-Layer Capacitor based on Carbon@ Covalent Organic Framework Aerogels

Jesús Á. Martín-Illán[+], Laura Sierra[+], Pilar Ocón, and Félix Zamora**

Abstract: High energy demand results in comprehensive research of novel materials for energy sources and storage applications. Covalent organic frameworks (COFs) possess appropriate features such as long-range order, permanent porosity, tunable pore size, and ion diffusion pathways to be competitive electrode materials. Herein, we present a deep electrochemical study of two COF-aerogels shaped into flexible COF-electrodes (ECOFs) by a simple compression method to fabricate an electrochemical double-layer capacitor (EDLC). This energy storage system has considerable interest owing to its high-power density and long cycle life compared with batteries. Our result confirmed the outstanding behavior of ECOFs as EDLC devices with a capacity retention of almost 100 % after 10000 charge/discharge cycles and, to our knowledge, the highest areal capacitance (9.55 $mF\,cm^{-2}$) in aqueous electrolytes at higher scan rates (1000 $mV\,s^{-1}$) for COFs. More importantly, the hierarchical porosity observed in the ECOFs increases ion transport, which permits a fast interface polarization (low τ_0 values). The complete sheds light on using ECOFs as novel electrode material to fabricate EDLC devices.

Introduction

Renewable energy sources are crucial to achieving a future sustainable economy.[1] These green-energy sources, such as solar energy, wind, hydro-energy, etc., show drawbacks associated with their intermittent availability. Therefore, energy storage components are a crucial part of renewable energy systems.[2] Nowadays, electrochemical double-layer capacitors (EDLCs) have attracted significant scientific attention in the energy storage field as promising energy storage devices because of their features, such as superior cycling stability, high power density, and fast charge/discharge rate.[3] EDCLs can quickly store and deliver much energy compared to batteries and pseudo-capacitors.[4] This feature of providing higher power density makes them suitable for widespread applications such as the acceleration of electric cars and emergency door openings in planes.[5] However, EDLC performance is limited by its electrode and electrolyte characteristics, such as chemical stability, continuous conductive pathways, and efficient mass transport channels.[6] In that sense, the most commonly used electrode materials are porous carbon structures (PCs) due to their abundance, non-toxic properties, high electrochemical stability, and conductivity.[7] Recently, two-dimensional (2D) materials have gained considerable interest for energy source applications owing to their tunable layer spacing, which can transport and host charge carriers.[8] Some 2D materials are good electronic conductors providing fast electronic transport and offering a high surface area for better electrode/electrolyte interface interaction. Graphene and its derivates single-/few-layer hexagonal sp^2-hybridized carbon nanosheets are the most studied 2D materials for electrochemical energy source applications because they have shown good performance as electrode materials for EDLCs.[7b,9] 2D fully π-conjugated aromatic structure gives graphene a large surface-to-volume ratio, high mechanical strength, outstanding electronic conductivity, and excellent chemical/electrochemical stability.[7a,10] However, no electron transfer takes place across the electrode/electrolyte interface during operation. This charge storage process is categorized as non-faradic. Moreover, graphene and PCs have been functionalized with redox actives sites to enhance electrochemical properties providing more capacitance by pseudocapacity or fast-Faradaic process.[11] In general, their performance is dramatically reduced during cyclability since limitations in transport and accessibility of ions.[12] Hence, the incorporation of porosity in graphene improves its

[*] J. Á. Martín-Illán,[+] Prof. F. Zamora
Departamento de Química Inorgánica, Universidad Autónoma de Madrid
28049 Madrid (Spain)
E-mail: felix.zamora@uam.es

L. Sierra,[+] P. Ocón
Departamento de Química-Fisica Aplicada, Universidad Autónoma de Madrid
28049 Madrid (Spain)
E-mail: pilar.ocon@uam.es

Prof. F. Zamora
Institute for Advanced Research in Chemical Sciences (IAdChem), Universidad Autónoma de Madrid
28049 Madrid (Spain)

[+] These authors contributed equally to this work.

charge storage performance. Still, the creation of such porosity is usually worked under harsh conditions, such as the chemical etching process with a vague tunable of porosity.[13] Notably, the difference between the electrolyte's size and electrode material's pores has been shown to be significant for achieving a high specific capacitance value in a carbon-based EDLC.[14] Thus, the processability of PCs into three-dimensional (3D) structures makes them promising candidates due to their hierarchical porosity that enhances ion transport.[15] Also, it has been shown that 3D morphologies with graphene improve mechanical strength and flexibility.[16] However, these materials are generally prepared by high-temperature treatment, i.e., pyrolysis, and their nano-/microstructure is hardly predictable and controllable.[9] Besides, there are many challenges to overcome, e.g., large-scale cost/efficient preparation of 3D graphene-based structures and self-supported high-performance electrode material.

Other 2D materials, such as transition metal oxides,[17] purely inorganic materials,[18] MXenes,[19] MOF,[20] and synthetic organic analogs to graphene as covalent organic frameworks (COFs), represent alternatives as active electrode materials to graphene and PCs.[21]

COFs are well-defined crystalline porous structures with long-range order and permanent porosity that Yaghi and co-workers first reported in 2005.[22] COFs have been extensively studied for proton,[23] electrical,[24] and charge carriers.[25] Moreover, their large surface areas make them promising candidates for energy storage and electrochemical application, especially for EDLC.[26] However, most COFs have been studied as pseudo-capacitor electrodes. As their whole structure is built up from organic building blocks connected by dynamic covalent bonds, COFs can show π-conjugated structures contributing to a modest electronic conductivity.[27] Incorporating functional groups onto the surface of the pore channel can boost their electrical conductivity, making them suitable for pseudo-capacitive energy storage.[26] For instance, Dichtel and co-workers fabricated for the first time a pseudo-capacitor with **DAAQ-TFP COF** (35 % wt.) and carbon black (65 % wt.).[28] Furthermore, the insoluble granular form in pristine COFs hinders their development as a stand-alone material and restricts their potential to be used for energy storage applications.[29] Hence, the processing of COF leads to the formation of thin films,[30] membranes,[31] thin sheets,[32] macroscopic composites,[33] and monoliths,[33b] providing versatility for the fabrication of novel energy storage devices.

In that sense, the processability of COFs into foams[34] or aerogels[35] facilities the mass transport of adsorbed molecules through their matrices. Thus, a synergistic effect was observed in which macropores are responsible for storing electrolyte ions, mesopores offer electrolyte ion transportation, and the intrinsic microstructure enables charge accommodation processes.[15]

Another aspect to consider is the interaction between electrodes/electrolytes, which play a crucial role in transferring and balancing charges between the two electrodes. Thus, selecting the correct electrolytes (organic or aqueous) is critical to achieving good device performance. Aqueous electrolytes give high conductivity and capacitance, but the ion mobility of aqueous electrolytes is affected by hydrated ion radius and pH. In contrast, organic media with alkylammonium salts have higher potential window stability, given high energy and power values.[36] However, poor accessibility of ions into the pores in the case of organic electrolytes induces similar values to the aqueous electrolyte.[36a,37]

However, the central role of COFs in electrochemical performance is to induce ion transport at the interface between the electrode and electrolyte because of their highly porous surface areas. The COF porosity increases the ion diffusion pathways, enhancing the performance of the devices. Additionally, a fully π-conjugated COF network will facilitate the charge transport, and its chemical and thermal stability will enlarge the cycling stability of the charge/discharge process. Finally, hierarchical porosity will be granted by the aerogel structure to improve ion and mass transfer, increasing the device's overall capacitance. Herein, we report flexible and mechanically robust symmetrical double-layer composite electrodes formed with imine-based COF-aerogels and 30 % wt. of Carbon Super P named **TAPB-BTCA-ECOF** and **TZ-BTCA-ECOF**.

As we recently reported, these COF-aerogels show a hierarchical porosity, low density (*ca.* 0.02 $g\,cm^{-3}$), and great mechanical properties.[35] Besides, their processing into free-standing COF membranes via a simple compression method preserves these mechanical and porosity features.[38] Thus, we studied the performance and the influence of ion size provided by different electrolytes of these promising COF-electrodes (**ECOFs**) working with different electrolytes: aqueous (H_2SO_4 1 $mol\,L^{-1}$, KOH 6 $mol\,L^{-1}$) and an organic electrolyte (tetrabutyl-ammonium hexafluorophosphate ($TBAPF_6$ 0.25 $mol\,L^{-1}$ in acetonitrile (ACN)). These **ECOFs** devices perform ideal double-layer charge storage at 100 $mV\,s^{-1}$ and achieve higher values of areal capacitance for aqueous electrolyte (11.2, and 8.96 $mF\,cm^{-2}$ for **TAPB-BTCA-ECOF** and **TZ-BTCA-ECOF**). In addition, these **ECOFs** devices show almost 100 % capacitance retention even after 10000 charge/discharge cycles with a high-power density of 2.0 $W\,cm^{-3}$. Additionally, to the best of our knowledge, the values of relaxation time constant (τ_0) are the lowest reported compared to carbon structures and COFs.[39] We postulate that **ECOFs** could become a considerable candidate material for EDLC devices by a simple compression method.

Results and Discussion

Following our previously reported method, we fabricated two structures of COF-electrodes based on COF-aerogels.[38] Firstly, the aerogels were gently broken into small pieces and mixed with 30 % wt. of Carbon Super P (Carbon-C65) in an agate mortar to enhance the electrical conductivity, obtaining a homogeneous composite mixture. Finally, the mixture was pressed under 120 MPa for 5 min, giving rise to a flexible free-standing electrode of the corresponding COF-

aerogels, named **TAPB-BTCA-ECOF** and **TZ-BTCA-ECOF** (Scheme 1). As we previously tested, we observed the influence of pressure on thickness and crystallinity, showing an optimal pressure at 120 MPa.[38] Moreover, we hypothesize that the lower density of COF-aerogels (*ca.* 0.02 g cm^{-3}) compared to their COF-powder counterparts is crucial for forming thinner COF-electrodes.

The **ECOFs** were characterized by Fourier transform infrared (FT-IR) spectroscopy, which confirmed the typical imine (C=N) stretching band at 1620 cm^{-1} (Section S3, Supporting Information). Additionally, characteristic vibrations of the amino and carbonyl groups of the precursors were detected, with a significant attenuation of the intensity at ca. ≈1690 cm^{-1} (C=O, stretching bands) and ≈3400 cm^{-1} (N–H, stretching bands), yet suggesting the presence of unreacted groups likely located at the defective edges of the COF nanolayers. Next, we turned to ^{13}C cross-polarized magic angle spinning solid-state NMR (^{13}C CP-MAS solid-state NMR), corroborated the formation of imine bonds at 156.3 ppm for **TAPB-BTCA-ECOF** and 154.4 ppm for **TZ-BTCA-ECOF**, and its triazine core also appears at 168 ppm (Section S4, Supporting Information).

The crystalline structure of **ECOFs** was confirmed by powder X-ray diffraction (PXRD) (Figures 1A and B). Indeed, **ECOFs** exhibited excellent crystallinity and matched with the simulated pattern of the AA-eclipsed stacking models. Thus, **TAPB-BTCA-ECOF** showed its corresponding peaks at 5.7°, 9.9°, and 11.5° attributed to the (100), (110), and (200) planes (Figure 1A). Similarly, **TZ-BTCA-ECOF** displayed the three peaks at 4.8°, 8.4°, and 9.8°, corresponding to the (100), (110), and (200) planes, respectively (Figure 1B). Thermogravimetric analysis (TGA) carried out under an N_2 atmosphere showed that the **ECOFs** are thermally stable up to 500 °C. Finally, the chemical stability of the **ECOFs** was evaluated upon immersion in aqueous solutions of sulfuric acid, H_2SO_4 1 mol L^{-1}, and potassium hydroxide, KOH 6 mol L^{-1}, respectively, at 333 K, with immersion times of 1 and 72 h (Section S6, Supporting Information). In the case of the alkaline solution, no significant changes were appreciated, but in the acid treatments, only 85 % of the solid material was recovered for **TAPB-BTCA-ECOF**, which could be associated with partial hydrolysis of the imine bond.[40]

Nitrogen sorption at 77 K of **ECOFs** was measured to demonstrate their permanent porosity (Section S7, Supporting Information). The isotherms for **TAPB-BTCA-ECOF** and **TZ-BTCA-ECOF** (Figures 1C and D) show a type IV sorption behavior related to mesoporous materials. The Brunauer–Emmett–Teller surface areas (SA_{BET}) of **ECOFs** 470 m^2 g^{-1} for **TAPB-BTCA-ECOF** and 565 m^2 g^{-1} for **TZ-BTCA-ECOF** (Section S7, Supporting Information) were measured. The contribution of Carbon Super P porosity was estimated to be 62 m^2 g^{-1}.[41] The pore size distributions were also calculated using the DFT method (Figures S18 and S22, Supporting Information). It is worth noting the hierarchical porosity display in the **ECOFs**, in which we can show the intrinsic structural pores of the framework and mesoporosity (2–50 nm) that are characteristic of the COF aerogel morphology (Table S4, Supporting Information).

The microstructure of the **ECOFs** was studied by scanning electron microscopy (SEM). SEM images show thicknesses in the range of 50–60 μm for **ECOFs** (Figures 1E and G); moreover, they display the formation of a continuous and homogeneous electrode (Figures 1F and H).

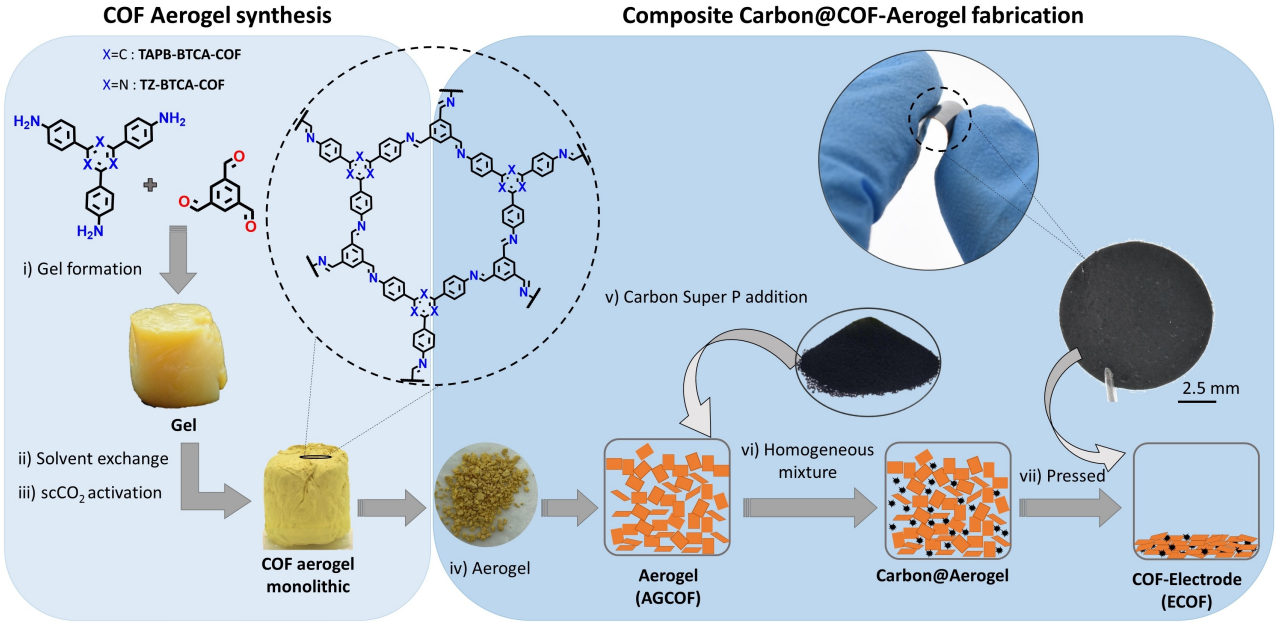

Scheme 1. Fabrication of COF-electrode (ECOFs) comprising; the synthesis of COF-aerogel via sol-gel processes; i) mixture of COF monomer in AcOH forming the COF-gels; ii) solvent exchange process, and iii) supercritical CO_2 ($scCO_2$) activation. Then, its processability by the compression method; iv) breaking COF-aerogel into small pieces; v) Carbon Super P addition; vi) homogeneous mixture of Carbon Super P and COF-aerogel; and vii) compression of the Carbon@COF aerogel composite. The photograph corresponds to the TZ-BTCA-ECOF.

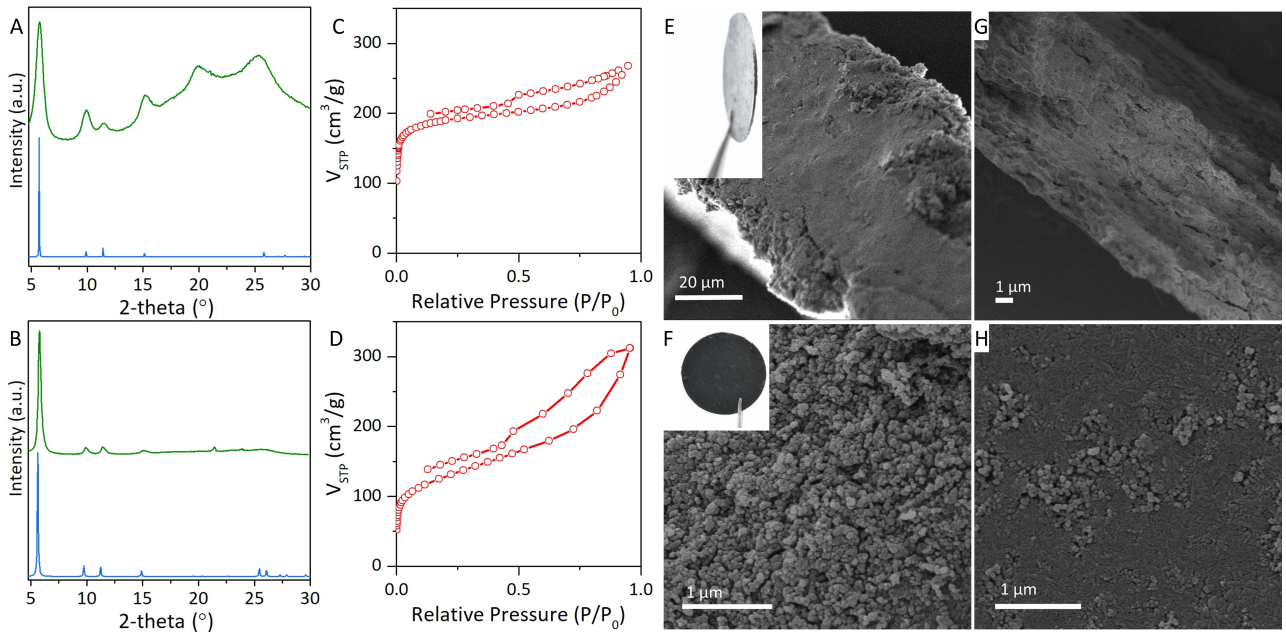

Figure 1. PXRD patterns of the corresponding ECOFs (green line), and simulated patterns (blue line) (A, B), N_2 adsorption-desorption isotherm for ECOFs (red line) (C, D), inset photographs of ECOFs (E, F) and SEM images (E, F, G, H) of TAPB-BTCA-ECOF (A, C, E, G) and TZ-BTCA-ECOF (B, D, F, H).

The presence of micropores or mesopores in the COF structures can lead to diffusion, i.e., mass transport limitations, which may hamper many applications and chemical reactions on electrodes. Thus, the incorporation in the material of larger pores (i.e., large mesopores and/or macropores) can provide unhindered mass transport to and from the electrode surface. Such a secondary porosity can be useful as the intrinsic structural porosity in crystalline COFs already offer large surface areas to enable fast surface reactions. Besides, in agreement with Pottathara et al.,[15] we suggest a different interaction of the different types of pore size distribution; macropores are responsible for storing electrolyte ions, mesopores offer ion transportation, and the intrinsic microstructure enables charge accommodation processes that increase the capacitance. So, such hierarchical porous systems, large surface areas, good mass transport, and distribution of active sites should facilitate applications in electrochemical reactions.

The electrical COF conductivity is usually too low for excellent electrochemical performance. So, it is necessary to incorporate electrical conductivity additives such as Carbon C65. It has been reported that van der Waals interactions between the COF backbone and the sp_2 carbon structure of the carbon black[21,42] promote efficient electron transfer through the composite, enhancing electrical conductivity.

To further check the interaction between Carbon-C65 and COF structure, we measured the electrical conductivity by a two-contact probe in a linear configuration of COF pristine in the form of membrane and **ECOFs** (Section S8, Supporting Information).[43] **TAPB-BTCA-ECOF** and **TZ-BTCA-ECOF** showed a conductivity of 5.4×10^{-3} S cm^{-1} and 4.1×10^{-3} S cm^{-1}, seven orders of magnitude greater than COF-aerogel (Table S5, Supporting Information). Therefore, once it demonstrated that **ECOFs** are crystalline, with permanent and hierarchical porosity, and flexible and good electrical conductivity, we evaluated their performance as EDLCs devices.

Firstly, we studied electrode/electrolyte interaction and divided electrolytes into aqueous and organic media. As we aforementioned, aqueous electrolytes showed high conductivity and capacitance due to OH^- and H^+ having no limitations in ion conductivity and higher conductivity values.[36] In contrast, organic media capacitance is limited by the dimension of quaternary ammonium ions of the tetrabutyl-ammonium salt and its solubility in ACN. Indeed, organic media show higher potential window stability than aqueous electrolytes.

In that sense, CV tests were performed to know the potential window stability of the electrolyte and analyze the capacitive behavior of the ECOFs devices. The three electrolytes that have been used for the electrochemical study were H_2SO_4 (1 mol L^{-1}), KOH (6 mol L^{-1}) as an aqueous electrolyte, and tetrabutyl-ammonium hexafluorophosphate ($TBAPF_6$ 0.25 mol L^{-1}, dried salt in ACN) as organic media.

Hence, the CV test of **ECOFs** showed an excellent electrochemical double-layer capacitor behavior for all media when we cycled at a scan rate of 100 mV s^{-1} (Figures 2A, B, and C). In addition, pseudo-capacity waves were not observed in aqueous media, confirming that double-layer charge storage was dominant. However, a small Faradaic-storage contribution was observed in the **TZ-BTCA-ECOF** device in organic media (Figure 2C) due to an interaction between the triazine core and $TBAPF_6$. Nevertheless, a non-Faradaic contribution dominates the storage mechanism.

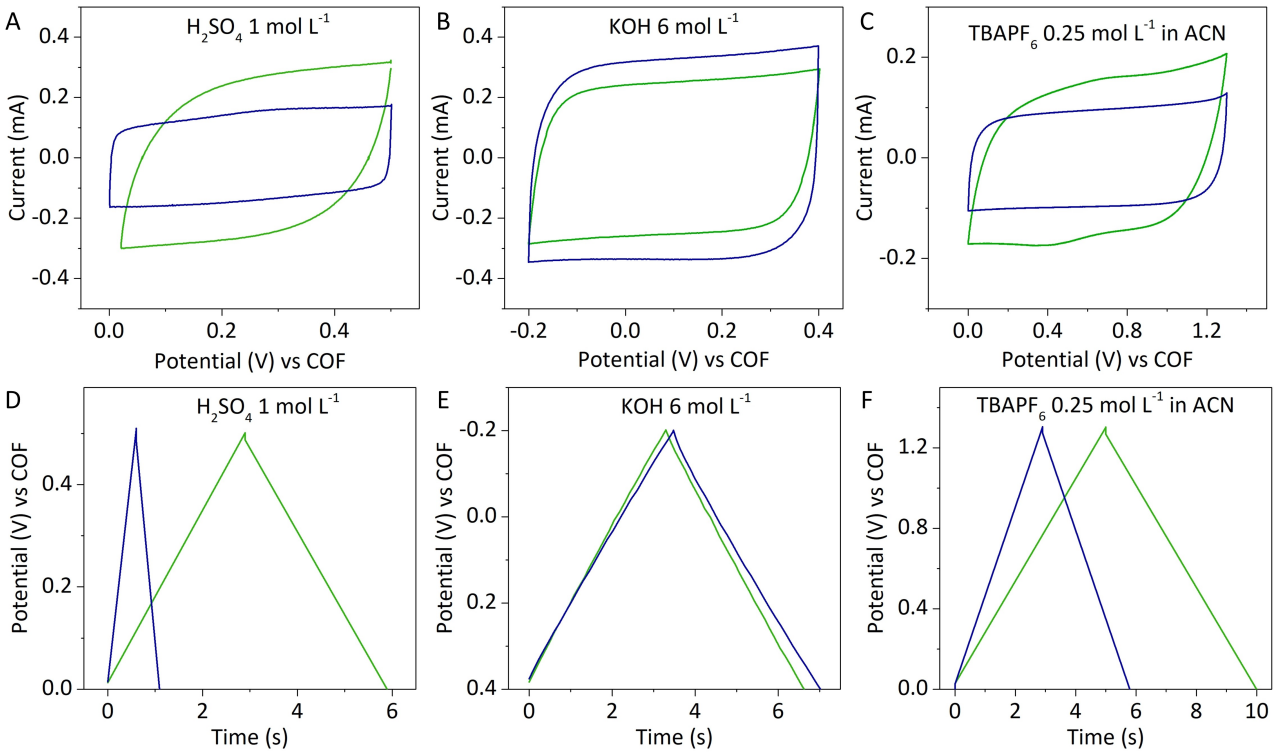

Figure 2. Cyclic voltammetry at 100 mV s^{-1} and 25 °C for TAPB-BTCA-ECOF (blue) and TZ-BTCA-ECOF (green) for three different electrolytes A) H_2SO_4 1 mol L^{-1}, B) KOH 6 mol L^{-1} and C) $TBAPF_6$ 0.25 mol L^{-1} in ACN. Galvanostatic charge/discharge at 0.1 A g^{-1} for (cycle 10000) TAPB-BTCA-ECOF (blue) and TZ-BTCA-ECOF (green) for three different electrolytes D) H_2SO_4 1 mol L^{-1}, E) KOH 6 mol L^{-1} and (F) $TBAPF_6$ 0.25 mol L^{-1} in ACN.

Additionally, we hypothesize that the hierarchical porosity observed in **ECOFs** enhanced the accessible surface area, increasing the ion diffusion. To demonstrate this theory, we evaluated charge storage capacity at higher scan rates with the same potential window (Section S9, Supporting Information).

Notably, an ideal capacitive behavior is observed even at 1000 mV s^{-1}, in which the rectangular shape is more remarkable and, consequently, the areal capacitance values are higher (Figure S27B, Supporting Information). It is important to know that conventional graphitic-carbon and COF-based capacitors generally operate at scan rates of 100–500 mV s^{-1}.[44] Nevertheless, an increased distortion from this ideal rectangular shape was observed at higher scan rates, which can be attributed to the inherent resistivity of the electrolyte ion penetration. The charge storage reaction became limited by the diffusion of the ions, so the device turned on more resistively with a capacity loss.

To further evaluate areal capacitance, we studied **ECOFs** devices cycled at a scan rate of 100 mV s^{-1} (Table S6, Supporting Information). Noteworthy, we obtained higher values of areal capacitance for aqueous electrolytes against the organic electrolyte (Table S7, Supporting Information). The best value was observed for KOH (Figure 2B), with values of 11.2 and 8.95 mF cm^{-2} for **TAPB-BTCA-ECOF** and **TZ-BTCA-ECOF** devices, respectively. On the other hand, the H_2SO_4 electrolyte performance showed a lower capacitance, 5.20 mF cm^{-2}, and 7.95 mF cm^{-2}, for **TAPB-BTCA-ECOF** and **TZ-BTCA-ECOF** devices. We associated capacitance reduction with the hydrolysis of the imine bond. Moreover, a breakup of **TAPB-BTCA-ECOF** was observed when it was added to the H_2SO_4 solution. Instead, **TZ-BTCA-ECOF** shows better values due to its higher chemical stability.[45] (Section S6, Supporting Information).

Meanwhile, the organic media areal capacitance is lower: 3.59 and 5.12 mF cm^{-2} for **TAPB-BTCA-ECOF** and **TZ-BTCA-ECOF** devices, respectively. In that case, the different performance can be attributed to a pseudo-capacitive contribution observed in **TZ-BTCA-ECOF**.[46]

It is worth noting that **TAPB-BTCA-ECOF** devices are managed at a high areal capacitance of 9.55 mF cm^{-2} at 1000 mV s^{-1} (Figure S27B, Supporting Information). Comparatively, this value is almost two times higher than, to our knowledge, the best value reported in COF for EDLC (e-JUC) 5.85 mF cm^{-2}, much higher than onion-like carbon (OLC) microcapacitor and other graphitic carbon capacitors (Table S9, Supporting Information).

Additionally, the influence of Carbon Super P was analyzed by CV (Section S2, Supporting Information). The areal capacitances obtained for carbon Super P are 2.14 and 0.58 mF cm^{-2} for KOH and H_2SO_4, respectively (Figure S30, Supporting Information). Considering that only 30 % wt. of our **ECOFs** is carbon, its capacitance contribution is not relevant enough for our electrochemical study.

Finally, to demonstrate the adaptability of **ECOFs** for practical applications in which devices are usually assembled

in series or parallel to get selected voltage or output current, two **TZ-BTCA-ECOF** devices in KOH were performed in series and parallel. (Figure S31, Supporting Information). In both configurations, **TZ-BTCA-ECOF** devices provided an almost ideal rectangular-shaped voltammogram), proving the stability and robustness of **ECOFs** devices. The device in series configuration increases power; meanwhile, in parallel design provides an increase in capacitance.

To further confirm the stability and reliability of **ECOFs** devices, galvanostatic charge/discharge (GCD) was tested at a constant current of $+/-0.1\,A\,g^{-1}$ for each electrolyte (Figures 2D, E, and F). Remarkably, both **ECOFs** devices showed nearly 100 % capacitance retention even after 10000 charge/discharge consecutive cycles (Figure S35 and Section S10, Supporting Information).

In that sense, potential-time curves are symmetrical, nearly triangular curves with low equivalent series resistance (ESR), as shown in Table S8 (Supporting Information), indicating the simultaneous and rapid charge/discharge.

The highest areal capacitance values were obtained for KOH; $8.00\,mF\,cm^{-2}$ and $7.45\,mF\,cm^{-2}$ for **TAPB-BTCA-ECOF** and **TZ-BTCA-ECOF** devices. However, the influence of the degradation of the material is observed for **TAPB-BTCA-ECOF** in the H_2SO_4 electrolyte, showing a lower value of $1.33\,mF\,cm^{-2}$ *vs* $8.05\,mF\,cm^{-2}$ for the **TZ-BTCA-ECOF** device, in agreement to the CV tests. On the other hand, the organic electrolyte shows areal capacitance of 3.05 and $5.25\,mF\,cm^{-2}$ for **TAPB-BTCA-ECOF** and **TZ-BTCA-ECOF** devices.

However, a deep study of the **TAPB-BTCA-ECOF** device in KOH at the 100th and 1000th of charge/discharge cycles displayed an instability that can be related to the interaction between KOH electrolyte and the terminals aldehydes of the nanolayers. These unreacted groups, likely located at the defective edges of the COF nanolayers created a pseudo-capacitance that disappeared after 1000 charge/discharge cycles (Figure S34B, Supporting Information). It was also observed for the **TZ-BTCA-ECOF** device. Nevertheless, **TZ-BTCA-ECOF** devices also showed significant changes in capacitance in the organic electrolyte, meaning a slight instability associated with the pseudo-capacitance behavior of triazine core, as shown in the CV.

To further confirm, different scan rates (0.3 and $0.6\,A\,g^{-1}$) were performed in the organic electrolyte for both **ECOFs** to analyze the influence of pseudo-capacitance (Figure S36, Supporting Information). The results showed a non-linear discharge at $0.3\,A\,g^{-1}$, typical pseudo-capacitive devices. These observations of instability will be explained in detail in the discussion of electrochemical impedance spectroscopy (EIS).

On the other hand, we evaluated COF-aerogel features *vs* a non-aerogel-based COF. Thus, we fabricated **ECOFs** based on COF-powder as a control measurement. The synthesis is achieved following the COF-aerogel synthetic procedure modifying the $scCO_2$ activation process by vacuum drying (Section S2, Supporting Information). Next, electrodes of the COF-powder (**powder-ECOFs**) were assembled following the compression method. However, the pressure needed to achieve homogeneous electrodes was much higher (*ca.* 300 MPa), which was also observed for COF-membranes.[38] Finally, we performed **powder-ECOFs** devices in KOH $6\,mol\,L^{-1}$, CV, and GCD evaluation showed a lower capacitance value for **powder-ECOFs** compared with **aerogel-ECOFs** counterparts (Figures S32 and S37, Supporting Information).

Next, we analyzed the double-layer capacitance and the efficient charge mobility within the **ECOFs** device. EIS was evaluated at zero time (before GCD), after 100 and 10000 charge/discharge cycles (Figure 3 and Section S11, Supporting Information). The Nyquist plot gives information about resistances associated with porous structures of electrodes and electrolytes (high frequency), ion transport limitation (middle frequency), and the total capacitance of the device (low frequency). Following previously reported for similar materials, the corresponding fitting to the equivalent series circuit (Figures 3A, B, D, and E) allows us to obtain the different EIS parameters for their interpretation.[47] The H_2SO_4 electrolyte was not evaluated due to the degradation of the material highlighted above, so EIS evaluation was done with KOH and $TBAPF_6$.

Firstly, in the high frequency, the element R_A represents the intercept on the real axis and gives information about the contribution of the resistances originated by the electrolyte, the intrinsic resistance of the electrode, and the contact resistance between the electrode material and the current collector.

The lowest values were obtained in KOH, 0.52 Ω, and 0.31 Ω (Figures 3A and D) *vs* values obtained for $TBAPF_6$, 10.0 Ω, and 12.0 Ω for **TAPB-BTCA-ECOF** and **TZ-BTCA-ECOF** device (Figures 3B and E). The results indicate great charge mobility within the electrodes, efficient ionic conductivity, and low internal electrode-electrolyte resistance.

The next element, R_B, is related to the resistance associated with the porous structure of the electrode. The difference between R_A and R_B is the diameter of the semicircle, which corresponds to R_P and reflects the penetration of the electrolyte into the pores. In KOH, **TAPB-BTCA-ECOF** R_B decreased from 6.8 to 3.8 Ω after 10000 cycles and slightly increased after 100 cycles (8 Ω), which indicates the requirement of time to achieve a regular performance.

As aforementioned in GCD, we associated this instability with the interaction between KOH and terminals aldehyde that affected ion diffusion. This interaction produces an increase in the resistance and the capacitance (Figure S34B, Supporting Information), but after charge/discharge cycles, we observed the resistance is reduced to 3.8 Ω, so we suggest a conversion of this terminal aldehyde into its corresponding alcohol or ion diffusion was not hind.

In contrast, for **TZ-BTCA-ECOF** devices R_B value is 4.0 Ω, and experiments showed no change after 10000 cycles. On the other hand, R_B for $TBAPF_6$ in **TAPB-BTCA-ECOF** devices is 125 and 85 Ω and for **TZ-BTCA-ECOF** devices is 627 and 257 Ω (before GCD and after 10000 cycles, respectively). R_B values are higher in the organic electrolyte for both **ECOFs**, which means that resistance of the electrolyte penetration is higher for both structures, and capacitance in that media is compromised. Also, there are

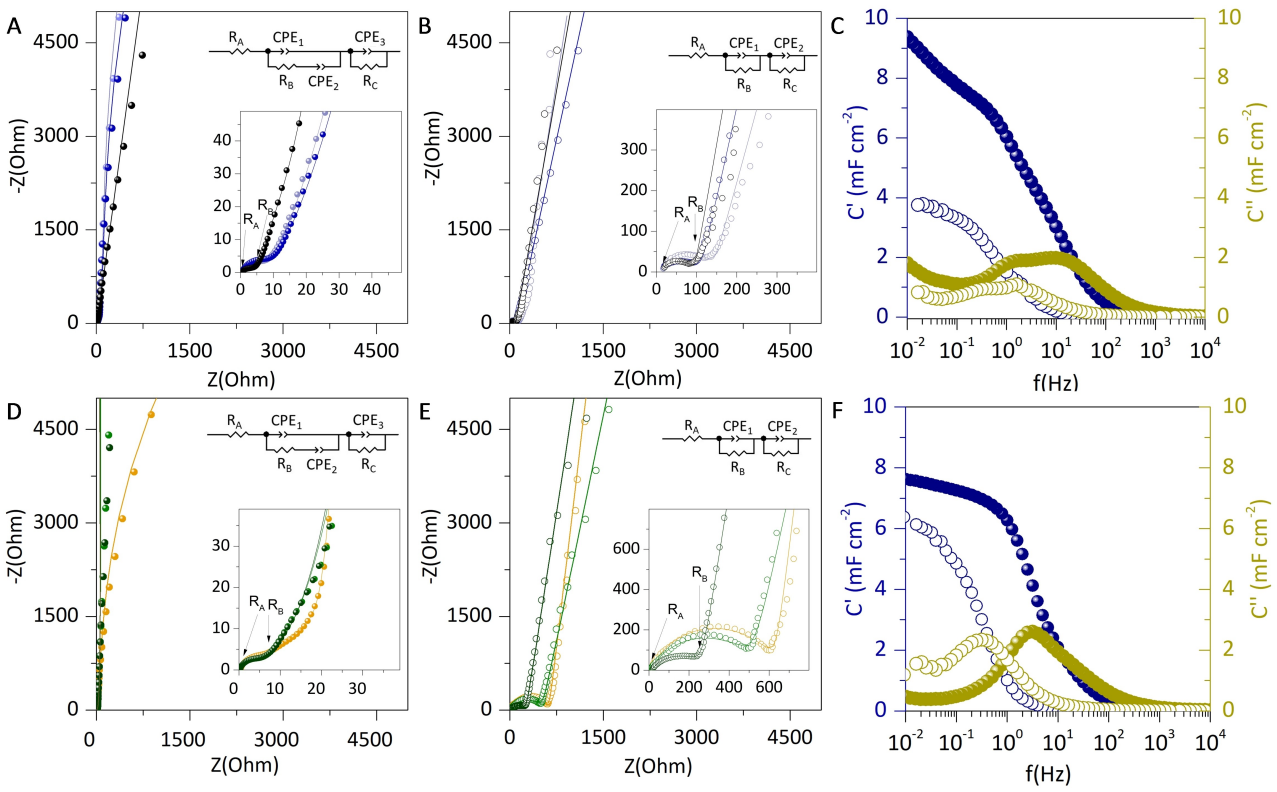

Figure 3. Nyquist Plot of A) TAPB-BTCA-ECOF in KOH, B) TAPB-BTCA-ECOF in $TBAPF_6$. Light blue dots are assigned to EIS measurement before charge/discharge, blue dots after 100 cycles charge/discharge, and black dots after 10000 cycles D) TZ-BTCA-ECOF in KOH, and E) TZ-BTCA-ECOF in $TBAPF_6$. Yellow dots are assigned to EIS measurement before charge/discharge, green dots after the first 100 cycles of charge/discharge, and dark green dots after 10000 cycles. C) C' and C'' versus frequency for TAPB-BTCA-ECOF (F) C' and C'' versus frequency for TZ-BTCA-ECOF. Dots correspond to KOH electrolyte, and circles correspond to $TBAPF_6$. For C and F, all measurements correspond to the EIS after 10000 cycles. The lines correspond to the fitting with the associated equivalent circuit for each measurement.

significate differences between both structures, **TZ-BTCA-ECOF** showed higher values of R_B. Also, changes were observed between 100 and 10000 cycles, with a significant decrease during the charge/discharge test. The highest values of R_B for **TZ-BTCA-ECOF** devices concerning **TAPB-BTCA-ECOF** devices can be associated with the pseudo-capacitive effect shown in CV performances and can affect the penetration of ions in the structure. Additionally, CPE_1 represents the double-layer capacitance related to the interface electrode-electrolyte.

In the middle frequency, CPE_2 corresponds to the diffusional behavior in KOH; the Nyquist plot shows a non-vertical line associated with the ion transport limitation of electrolyte in porous electrodes, indicating the access of the ions in the electrode leading to an increase of the capacitance.[48] When n_2 of the CPE is near 0.5 the diffusional part could be simulated as a Warburg element. We cannot observe the diffuse layer resistance in the organic electrolyte, and the circuit is simplified by removing this CPE_2. The absence of the diffusional part means no diffusion limit over the electrode/electrolyte interfaces. This can be associated with the high resistance of the tetrabutylammonium ion to access the microporous **ECOF** devices; therefore, capacitance behavior is related to mesoporous porosity.

Next, the second circuit in the series is constituted by a CPE_3/R_C denoting **ECOF** capacitance and leakage resistance behavior in the low frequency. The Nyquist plot shows a vertical line attributed mainly to the capacitive contribution of the double layer formed by the electrode/electrolyte. The value of CPE_3 obtained by fitting gives information about capacitive behavior and indicates the ideal capacitive behavior when n_3 is near 1.

Following the previous results by CV test and GCD performances, the capacitance contribution value obtained from CPE_3-T for aqueous electrolytes were 6.5 $mF\,cm^{-2}$ and 4.35 $mF\,cm^{-2}$ for **TAPB-BTCA-ECOF** and **TZ-BTCA-ECOF** devices. Indeed, for the organic electrolyte, n_3 is between 0.89–0.9, with a capacitance value of 1.41 and 2.58 $mF\,cm^{-2}$ for **TAPB-BTCA-ECOF** and **TZ-BTCA-ECOF** devices (Table S10, Supporting Information).

The complex capacitance plots can analyze the performance of energy conversion devices as described by different authors.[49] The real and imaginary part of the complex capacitance is calculated using the following equations:

$$C(w) = C'(w) + C''(w) \quad (1)$$

$$C' = \frac{-Z''(w)}{w\left|Z(w)^2\right|} \tag{2}$$

$$C'' = \frac{-Z'(w)}{w\left|Z(w)^2\right|} \tag{3}$$

C' is the real part of complex capacitance and C'' is the imaginary part and can be expressed by equations (Figures 4A and B). The representation of C' and C'' vs f(Hz) provide information about the relaxation time (τ_0) and the maximum capacitance in the minimum frequency (0.01 Hz).[49] The evolution of C'' vs frequency shows a maximum at the frequency f_0, which defines $\tau_0 = 1f_0^{-1}$ (Figures 3C and F).[47b] This parameter represents the minimum time needed to discharge all the energy from the electrode with an efficiency higher than 50 %.[49] For the aqueous electrolyte (KOH), after 10000 charge/discharge cycles, τ_0 was 50 and 79 ms for **TAPB-BTCA-ECOF** and **TZ-BTCA-ECOF** (Figures 3C and F).

This value indicates that the symmetric cell can be fully charged within a relatively short period. In contrast, for the organic electrolyte, as we previously showed, the resistance diffusion of the ions was higher; therefore, the capacitance behavior began in lower frequencies, and τ_0 values were higher, 480 and 2100 ms for **TAPB-BTCA-ECOF** and **TZ-BTCA-ECOF**. Despite this, a higher value of τ_0 for **TZ-BTCA-ECOF** in the organic media can be related to the pseudo-capacitance contribution, as previously commented.

For KOH, τ_0 values of our **ECOFs** devices were lower compared to carbon-based capacitors, with values of 700 ms,[39b] and 188 ms,[39a] indicating faster ion diffusivity. The lower values of τ_0 confirmed ion diffusion is enhanced by accessible surface area proportionated by hierarchical porosity. Another method to calculate τ_0 can be done by plotting the phase angle versus the frequency, $\tau_0 = (1\ f_0^{-1})$. It represents the bode plots of both **ECOFs** devices in alkaline and organic electrolyte (Figures S38 and S39, Supporting Information). The frequency value corresponds to a phase angle of −45° and gives information about τ_0.

Finally, to complete a deeper characterization of **ECOFs** devices is indispensable to know the complex power (S), which represents the electrical power in a complex number; the real part is represented by active power (P), whereas the imaginary part is represented by the reactive power (Q).

$$S = P + jQ \tag{4}$$

And the active power (P) and reactive power (Q) can be described as:

$$P(w) = wC''(w)|\Delta Vrms|^2 \tag{5}$$

$$Q(w) = wC'(w)|\Delta Vrms|^2 \tag{6}$$

At high frequency, when the capacitor behaves as a pure resistance, all the power is dissipated into the system ($P = 100\,\%$), while no power is dissipated into a pure capacitance at low frequency. As has been previously commented, the aqueous electrolytes exhibit higher capacitance and lower τ_0 indicating better ion conductivity.

In that sense, in Figure 4, we observe a pure capacity contribution of **ECOFs** devices in aqueous electrolytes that hold 100 % of power in lower frequencies (f→0) and dissipate at higher frequencies (≈1 Hz). In contrast, organic electrolytes dissipated power in frequencies below 0.3 and 0.1 Hz for **TAPB-BTCA-ECOF** and **TZ-BTCA-ECOF**. On the other hand, the charge/discharge time constant ($\tau_0 = 1/f_0$) determined at the resonant frequency corresponds to the phase angle of 45°, which represents the transition for the electrochemical capacitor between a pure resistive ($f > 1/\tau_0$) and a pure capacitive ($f < 1/\tau_0$) behavior. The intersection between |P/S| and |Q/S| (Figure 4) is the frontier between the capacitive and resistive behavior. For the aqueous electrolyte, τ_0 values of 0.04 s and 0.08 s were obtained for **TAPB-BTCA-ECOF** and **TZ-BTCA-ECOF** devices. In contrast, **ECOFs** devices in organic electrolytes dissipate the power at lower frequencies with τ_0 values of 0.48 s and 2.1 s for **TAPB-BTCA-ECOF** and **TZ-BTCA-ECOF** associated with lower capacitance performance. The three different methods to obtain τ_0 displayed similar values.

In general, this representation is evidence of the higher storage and faster time of charge/discharge of **ECOFs** devices in aqueous electrolytes. These promising results

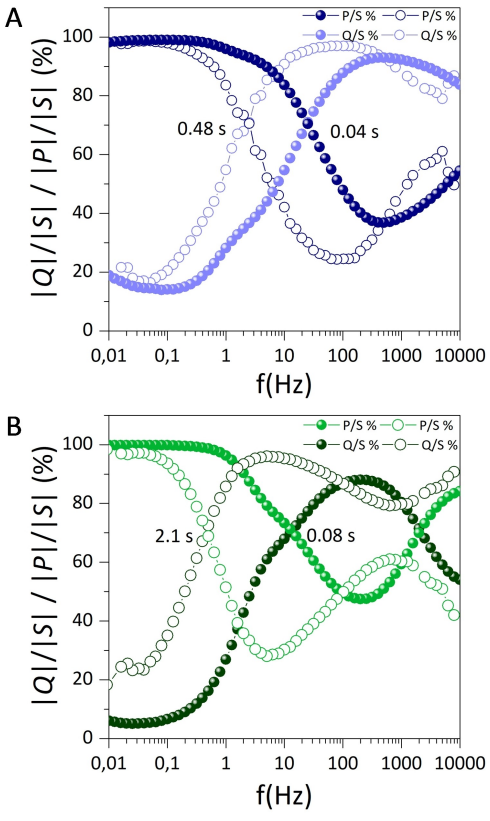

Figure 4. Normalized reactive power |Q|/|S| and active power |P|/|S| vs frequency for A) TAPB-BTCA ECOF in KOH 6 mol L^{-1} (blue dots), $TBAPF_6$ 0.25 mol L^{-1} in ACN (blue circles). B) TZ-BTCA-ECOF in KOH 6 mol L^{-1} (green dots), $TBAPF_6$ 0.25 mol L^{-1} in ACN (green circles). All measurements correspond to the EIS after 10000 cycles.

reveal the reliable performance of **ECOFs** devices as candidates for EDLC.

Conclusion

In summary, we have reported a simple compression method to fabricate flexible, hierarchical porous COF-electrodes based on Carbon@COF-aerogels composite for EDLC devices. The engineering shaping of COF-aerogel and their processing to **ECOFs** provides a highly porous surface with a hierarchical porosity that enhances the ion transport at the interface of the electrode since its increases the ion diffusion pathways giving rise to elevate performance rates of the device. The deeper electrochemical study showed the influence of three electrolytes; aqueous electrolytes (H_2SO_4 and KOH) and organic electrolyte ($TBAPF_6$ in acetonitrile) with both **ECOFs** structures, showing that the presence of triazine core in **TZ-BTCA-ECOF** structure is not remarkable for KOH, while for organic electrolyte is observed with a pseudocapacitive behavior, that enhances their capacitance in comparison with the alternative structure.

The features of COF-aerogel moved to **ECOFs**, such as a highly porous surface with a wide pore size distribution, provided EDLC devices the lowest τ_0 reported in COF-based capacitors (50 ms), indicating a high-speed ion diffusivity. The synergic effect between **ECOF** and electrolyte was also observed in the capacitance values, obtaining the best in KOH electrolyte (11.2 $mF\,cm^{-2}$), and the best power (2.0 $W\,cm^{-3}$) and energy values (0.11 $mWh\,cm^{-3}$) in organic electrolyte. Furthermore, the covalently linked network brings good stability and outstanding cyclability (98 % capacitance retention over 10000 charge/discharge cycles) for all the electrolytes. We believe that these electrochemical studies indicate the limiting factor electrode structure/electrolyte to consider the design of a non-Faradaic device. Additionally, this simple procedure to fabricate **ECOFs** holds a great perspective in developing high-performance EDLC devices and, with an improvement process, micro-EDLC.

Acknowledgements

This work has been supported by the Spanish MINECO (PID2019-106268GB-C32) and through the "María de Maeztu" Programme for Units of Excellence in R&D (CEX2018-000805-M).

Conflict of Interest

The authors declare no conflict of interest.

Data Availability Statement

The data that support the findings of this study are openly available in UAM repository at https://repositorio.uam.es/handle/10486/13424.

Keywords: Aerogels · Covalent Organic Frameworks · Flexible Electrodes · Porous Materials

[1] S. Chu, A. Majumdar, *Nature* **2012**, *488*, 294–303.
[2] Z. Yang, J. Zhang, M. C. Kintner-Meyer, X. Lu, D. Choi, J. P. Lemmon, J. Liu, *Chem. Rev.* **2011**, *111*, 3577–3613.
[3] a) N. Wu, X. Bai, D. Pan, B. Dong, R. Wei, N. Naik, R. R. Patil, Z. Guo, *Adv. Mater. Interfaces* **2021**, *8*, 2001710; b) P. Naskar, A. Maiti, P. Chakraborty, D. Kundu, B. Biswas, A. Banerjee, *J. Mater. Chem. A* **2021**, *9*, 1970–2017.
[4] Y. Wang, Y. Song, Y. Xia, *Chem. Soc. Rev.* **2016**, *45*, 5925–5950.
[5] L. Zhang, X. Hu, Z. Wang, F. Sun, D. G. Dorrell, *Renewable Sustainable Energy Rev.* **2018**, *81*, 1868–1878.
[6] M. Yu, R. Dong, X. Feng, *J. Am. Chem. Soc.* **2020**, *142*, 12903–12915.
[7] a) Y. Shao, M. F. El-Kady, L. J. Wang, Q. Zhang, Y. Li, H. Wang, M. F. Mousavi, R. B. Kaner, *Chem. Soc. Rev.* **2015**, *44*, 3639–3665; b) Y. B. Tan, J.-M. Lee, *J. Mater. Chem. A* **2013**, *1*, 14814–14843.
[8] X. Zhang, L. Hou, A. Ciesielski, P. Samorì, *Adv. Energy Mater.* **2016**, *6*, 1600671.
[9] M. A. Al Faruque, M. Syduzzaman, J. Sarkar, K. Bilisik, M. Naebe, *Nanomaterials* **2021**, *11*, 2414.
[10] J. Zhu, D. Yang, Z. Yin, Q. Yan, H. Zhang, *Small* **2014**, *10*, 3480–3498.
[11] X. Yu, S. Yun, J. S. Yeon, P. Bhattacharya, L. Wang, S. W. Lee, X. Hu, H. S. Park, *Adv. Energy Mater.* **2018**, *8*, 1702930.
[12] J. Romero, D. Rodriguez-San-Miguel, A. Ribera, R. Mas-Ballesté, T. F. Otero, I. Manet, F. Licio, G. Abellán, F. Zamora, E. Coronado, *J. Mater. Chem. A* **2017**, *5*, 4343–4351.
[13] L. L. Zhang, X. Zhao, M. D. Stoller, Y. Zhu, H. Ji, S. Murali, Y. Wu, S. Perales, B. Clevenger, R. S. Ruoff, *Nano Lett.* **2012**, *12*, 1806–1812.
[14] V. S. Kale, M. Hwang, H. Chang, J. Kang, S. I. Chae, Y. Jeon, J. Yang, J. Kim, Y.-J. Ko, Y. Piao, T. Hyeon, *Adv. Funct. Mater.* **2018**, *28*, 1803786.
[15] Y. B. Pottathara, H. R. Tiyyagura, Z. Ahmad, K. K. Sadasivuni, *J. Energy Storage* **2020**, *30*, 101549.
[16] P. Xie, W. Yuan, X. Liu, Y. Peng, Y. Yin, Y. Li, Z. Wu, *Energy Storage Mater.* **2021**, *36*, 56–76.
[17] J. Wei, X. Li, H. Xue, J. Shao, R. Zhu, H. Pang, *Adv. Mater. Interfaces* **2018**, *5*, 1701509.
[18] a) Y. Lu, B. Li, S. Zheng, Y. Xu, H. Xue, H. Pang, *Adv. Funct. Mater.* **2017**, *27*, 1703949; b) B. Vidhyadharan, I. I. Misnon, R. A. Aziz, K. P. Padmasree, M. M. Yusoff, R. Jose, *J. Mater. Chem. A* **2014**, *2*, 6578–6588.
[19] M. Hu, H. Zhang, T. Hu, B. Fan, X. Wang, Z. Li, *Chem. Soc. Rev.* **2020**, *49*, 6666–6693.
[20] D. Sheberla, J. C. Bachman, J. S. Elias, C. J. Sun, Y. Shao-Horn, M. Dinca, *Nat. Mater.* **2017**, *16*, 220–224.
[21] X. Zhao, P. Pachfule, A. Thomas, *Chem. Soc. Rev.* **2021**, *50*, 6871–6913.
[22] a) C. S. Diercks, O. M. Yaghi, *Science* **2017**, *355*, eaal1585; b) A. P. Cote, A. I. Benin, N. W. Ockwig, M. O'Keeffe, A. J. Matzger, O. M. Yaghi, *Science* **2005**, *310*, 1166–1170.
[23] S. Chandra, T. Kundu, S. Kandambeth, R. Babarao, Y. Marathe, S. M. Kunjir, R. Banerjee, *J. Am. Chem. Soc.* **2014**, *136*, 6570–6573.

[24] S. Jin, M. Supur, M. Addicoat, K. Furukawa, L. Chen, T. Nakamura, S. Fukuzumi, S. Irle, D. Jiang, *J. Am. Chem. Soc.* **2015**, *137*, 7817–7827.
[25] S. Ghosh, Y. Tsutsui, T. Kawaguchi, W. Matsuda, S. Nagano, K. Suzuki, H. Kaji, S. Seki, *Chem. Mater.* **2022**, *34*, 736–745.
[26] S. Kandambeth, V. S. Kale, O. Shekhah, H. N. Alshareef, M. Eddaoudi, *Adv. Energy Mater.* **2022**, *12*, 2100177.
[27] T. Sun, J. Xie, W. Guo, D.-S. Li, Q. Zhang, *Adv. Energy Mater.* **2020**, *10*, 1904199.
[28] C. R. DeBlase, K. E. Silberstein, T. T. Truong, H. D. Abruna, W. R. Dichtel, *J. Am. Chem. Soc.* **2013**, *135*, 16821–16824.
[29] D. Rodríguez-San-Miguel, F. Zamora, *Chem. Soc. Rev.* **2019**, *48*, 4375–4386.
[30] B. Hosseini Monjezi, K. Kutonova, M. Tsotsalas, S. Henke, A. Knebel, *Angew. Chem. Int. Ed.* **2021**, *60*, 15153–15164; *Angew. Chem.* **2021**, *133*, 15281–15293.
[31] C. Fan, H. Wu, J. Guan, X. You, C. Yang, X. Wang, L. Cao, B. Shi, Q. Peng, Y. Kong, Y. Wu, N. A. Khan, Z. Jiang, *Angew. Chem. Int. Ed.* **2021**, *60*, 18051–18058; *Angew. Chem.* **2021**, *133*, 18199–18206.
[32] A. Khayum M, V. Vijayakumar, S. Karak, S. Kandambeth, M. Bhadra, K. Suresh, N. Acharambath, S. Kurungot, R. Banerjee, *ACS Appl. Mater. Interfaces* **2018**, *10*, 28139–28146.
[33] a) N. An, Z. Guo, J. Xin, Y. He, K. Xie, D. Sun, X. Dong, Z. Hu, *J. Mater. Chem. A* **2021**, *9*, 16824–16833; b) C. Li, J. Yang, P. Pachfule, S. Li, M. Y. Ye, J. Schmidt, A. Thomas, *Nat. Commun.* **2020**, *11*, 4712.
[34] S. Karak, K. Dey, A. Torris, A. Halder, S. Bera, F. Kanheerampockil, R. Banerjee, *J. Am. Chem. Soc.* **2019**, *141*, 7572–7581.
[35] J. A. Martin-Illán, D. Rodriguez-San-Miguel, O. Castillo, G. Beobide, J. Perez-Carvajal, I. Imaz, D. Maspoch, F. Zamora, *Angew. Chem. Int. Ed.* **2021**, *60*, 13969–13977; *Angew. Chem.* **2021**, *133*, 14088–14096.
[36] a) S. Vaquero, R. Díaz, M. Anderson, J. Palma, R. Marcilla, *Electrochim. Acta* **2012**, *86*, 241–247; b) B. Pal, S. Yang, S. Ramesh, V. Thangadurai, R. Jose, *Nanoscale Adv.* **2019**, *1*, 3807–3835.
[37] R. Mysyk, E. Raymundo-Piñero, J. Pernak, F. Béguin, *J. Phys. Chem. C* **2009**, *113*, 13443–13449.
[38] J. A. Martin-Illán, J. A. Suarez, J. Gomez-Herrero, P. Ares, D. Gallego-Fuente, Y. Cheng, D. Zhao, D. Maspoch, F. Zamora, *Adv. Sci.* **2022**, *9*, 2104643.
[39] a) P. K. Jha, S. K. Singh, V. Kumar, S. Rana, S. Kurungot, N. Ballav, *Chem* **2017**, *3*, 846–860; b) D. Pech, M. Brunet, H. Durou, P. Huang, V. Mochalin, Y. Gogotsi, P.-L. Taberna, P. Simon, *Nat. Nanotechnol.* **2010**, *5*, 651–654.
[40] A. Halder, S. Karak, M. Addicoat, S. Bera, A. Chakraborty, S. H. Kunjattu, P. Pachfule, T. Heine, R. Banerjee, *Angew. Chem. Int. Ed.* **2018**, *57*, 5797–5802; *Angew. Chem.* **2018**, *130*, 5899–5904.
[41] K. Pfeifer, S. Arnold, Ö. Budak, X. Luo, V. Presser, H. Ehrenberg, S. Dsoke, *J. Mater. Chem. A* **2020**, *8*, 6092–6104.
[42] a) J. Xu, Y. He, S. Bi, M. Wang, P. Yang, D. Wu, J. Wang, F. Zhang, *Angew. Chem. Int. Ed.* **2019**, *58*, 12065–12069; *Angew. Chem.* **2019**, *131*, 12193–12197; b) A. K. Mohammed, V. Vijayakumar, A. Halder, M. Ghosh, M. Addicoat, U. Bansode, S. Kurungot, R. Banerjee, *ACS Appl. Mater. Interfaces* **2019**, *11*, 30828–30837.
[43] L. Sun, S. S. Park, D. Sheberla, M. Dincă, *J. Am. Chem. Soc.* **2016**, *138*, 14772–14782.
[44] Y. Yusran, H. Li, X. Guan, D. Li, L. Tang, M. Xue, Z. Zhuang, Y. Yan, V. Valtchev, S. Qiu, Q. Fang, *Adv. Mater.* **2020**, *32*, 1907289.
[45] J. Dong, Y. Wang, G. Liu, Y. Cheng, D. Zhao, *CrystEngComm* **2017**, *19*, 4899–4904.
[46] L. Li, F. Lu, R. Xue, B. Ma, Q. Li, N. Wu, H. Liu, W. Yao, H. Guo, W. Yang, *ACS Appl. Mater. Interfaces* **2019**, *11*, 26355–26363.
[47] a) S. Guo, H. Li, X. Zhang, H. Nawaz, S. Chen, X. Zhang, F. Xu, *Carbon* **2021**, *174*, 500–508; b) B. Véliz, S. Bermejo, A. Orpella, L. Castañer, *Electrochim. Acta* **2018**, *280*, 62–70.
[48] B.-A. Mei, O. Munteshari, J. Lau, B. Dunn, L. Pilon, *J. Phys. Chem. C* **2018**, *122*, 194–206.
[49] P. L. Taberna, P. Simon, J. F. Fauvarque, *J. Electrochem. Soc.* **2003**, *150*, A292.

Manuscript received: September 5, 2022
Accepted manuscript online: October 3, 2022
Version of record online: ■■, ■■

Research Articles

Covalent Organic Frameworks

J. Á. Martín-Illán, L. Sierra, P. Ocón,*
F. Zamora* ——— e202213106

Electrochemical Double-Layer Capacitor based on Carbon@ Covalent Organic Framework Aerogels

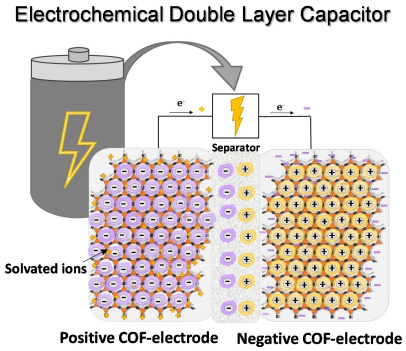

Covalent organic framework (COFs) aerogels are shaped into flexible electrode composite by a simple compression method. It shows permanent porosity and great ion diffusion pathways appropriated for electrochemical double-layer capacitors (EDLC). These EDLC devices demonstrated a significant areal capacitance (11.2 mF cm^{-2}) with the lowest τ_0 reported in COF-based capacitors, 50 ms, and a 98% capacitance retention over 10000 charge/discharge cycles.